Nanoscale

ROYAL SOCIETY OF CHEMISTRY

MINIREVIEW

View Article Online
View Journal | View Issue

Cite this: *Nanoscale*, 2023, **15**, 7249

All-inorganic perovskite solar cells featuring mixed group IVA cations

Yufeng Li,[a] Changyu Yang,[b] Weisi Guo,[a] Tianwei Duan,*[b] Zhongmin Zhou *[a] and Yuanyuan Zhou *[b]

Received 9th January 2023,
Accepted 19th February 2023

DOI: 10.1039/d3nr00133d

rsc.li/nanoscale

All-inorganic perovskites are promising for solar cells owing to their potentially superior tolerance to environmental factors, as compared with their hybrid organic–inorganic counterparts. Over the past few years, all-inorganic perovskite solar cells (PSCs) have seen a dramatic improvement in certified power conversion efficiencies (PCEs), demonstrating their great potential for practical applications. Pb, Sn, and Ge are the most studied group IVA elements for perovskites. These group IVA cations share the same number of valence electrons and similarly exhibit the beneficial antibonding properties of lone-pair electrons when incorporated in the perovskite structure. Meanwhile, mixing these cations in all-inorganic perovskites provides opportunities for stabilizing the photoactive phase and tailoring the bandgap structure. In this mini-review, we analyze the structural and bandgap design principles for all-inorganic perovskites featuring mixed group IVA cations, discuss the updated progress in the corresponding PSCs, and finally provide perspectives on future research efforts faciliating the continued development of high-performance Pb-less and Pb-free all-inorganic PSCs.

Introduction

Perovskite solar cells (PSCs) are attractive alternatives to commercial silicon-based solar cells owing to their low-cost fabrication processes and high power conversion efficiencies (PCEs). Metal halide perovskite materials based on common ABX_3 crystal structures exhibit diverse chemical composition space and large tolerance in structural disorder, as well as numerous photophysical merits, such as high absorption coefficients, long carrier diffusion lengths, and low exciton binding energies.[1–15] Since the first study by Miyasaka and coworkers in 2009, the PCEs of PSCs have skyrocketed from 3.8% to 25.7%.[16,17] Nevertheless, the state-of-the-art PSCs mainly employ hybrid organic–inorganic perovskites entailing organic A-site cations including $CH_3NH_3^+$ (MA^+) and/or $CH(NH_2)_2^+$ (FA^+), while the future commercial applications of organic–inorganic perovskites are hampered by their poor stability under light, thermal, and moisture conditions. The research on all-inorganic perovskites demonstrates an important strategy to

[a]College of Chemistry and Molecular Engineering, Qingdao University of Science and Technology, Qingdao 266042, P. R. China. E-mail: zhouzm@qust.edu.cn
[b]Department of Physics, Hong Kong Baptist University, Kowloon, Hong Kong SAR, P. R. China. E-mail: duantw@hkbu.edu.hk, yyzhou@hkbu.edu.hk

Yufeng Li

Yufeng Li is currently a research graduate student at Qingdao University of Science and Technology. He obtained his B.S. degree from Qingdao University of Science and Technology in 2020. His current research focuses on obtaining highly efficient and stable perovskite solar cells through interfacial engineering.

Changyu Yang

Changyu Yang is currently a Research Assistant in the Advanced Semiconductor Laboratory (ΣLab) at Hong Kong Baptist University. He received his bachelor's degree (2019) in Functional Materials from Donghua University and master's degree (2022) in Materials Science from the University of Southern California. His research currently focuses on microstructure in perovskite optoelectronics.

mitigate the stability issue for hybrid organic–inorganic PSCs, which is attributed to the replacement of organic A-site cations with inorganic Cs cations.[18–24] The most representative all-inorganic PSCs are based on $CsPbI_{3-x}Br_x$ (x = 0–3), which have been developed rapidly owing to their combined features of more appropriate bandgaps and potentially better stability.[25] The best $CsPbI_{3-x}Br_x$ PSCs have delivered PCEs of >20% and meanwhile, superior environmental stability is shown compared to their hybrid organic–inorganic counterparts.[26] Regardless of the promising development of $CsPbI_{3-x}Br_x$ PSCs, the occupation of Pb cations in all B-sites of perovskites raises a concern about toxicity, which need to be considered for the future commercialization.[27] In this context, the development of all-inorganic PSCs using Pb-less or Pb-free perovskites is important, as it can unlock a possiblity to simultaneously enhance the PCE, stability, and environment-friendliness. Sn and Ge are the two elements that are within the group IVA like Pb but with much less metal toxicity. Since both of them have the same number of valence electrons, Sn and Ge cations are excellent candidates for the partial or complete replacement of Pb cations in the B-sites of perovskite crystal structures, maintaining the beneficial antibonding properties of lone-pair electrons in pure Pb-based perovskites.

While recently excellent review works have been done to summarize the research progress in all-inorganic Pb-based PSCs[28–33] and all-inorganic Pb-free PSCs[34–37] from the perspective of stability and efficiency enhancements, this mini-review mainly focuses on the updated development of all-inorganic Pb-less or Pb-free PSCs *via* the strategy of mixed group IVA cations, which can represent a new angle of view. In this work, we will first provide a fundamental discussion of perovskites with mixed group IVA cations regarding their crystal and electronic band structures, then summarize the film optimization strategies for the resulting PSCs, and finally indicate promising research directions for developing all-inorganic perovskite solar cells featuring mixed group IVA cations.

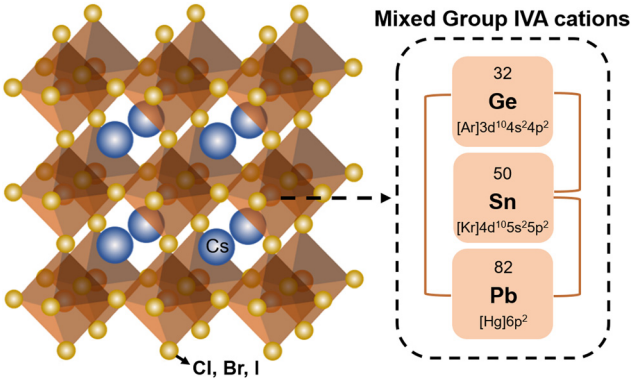

Fig. 1 Crystal structure of the all-inorganic ABX_3 perovskite based on mixed group IVA cations.

Design principle

Crystal structure

The general chemical formula of all-inorganic perovskites based on mixed group IVA cation is ABX_3, where A is a monovalent cation (*e.g.* Cs^+), B is a divalent cation (*e.g.* Pb^{2+}, Sn^{2+}, Ge^{2+}), and X is a halide ion (*e.g.* I^-, Br^-). The ideal crystal structure of ABX_3 can be regarded as a grid-like framework composed of BX_6-octahedra connected at the corner-sharing vertices in three-dimensional space, and a large A-site is in the voids of a dodecahedron (Fig. 1). The structural stability of perovskites with various compositions can be given empirically by the Goldschmidt tolerance factor (t),[38]

$$t = \frac{R_A + R_X}{\sqrt{2}(R_B + R_X)} \quad (1)$$

where R_A, R_B, and R_X refer to the radii of the A, B, and X cations, respectively. When t equals 1, the crystal structure of the perovskite is an ideal cubic phase ($Pm3m$).

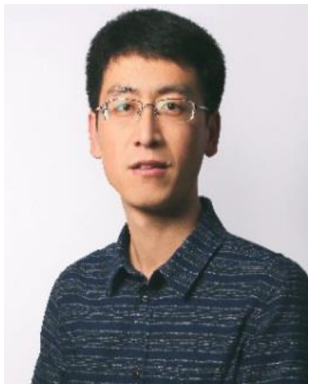

Weisi Guo

Weisi Guo received his B.S. and M.S. degrees from Qingdao University of Science and Technology. He obtained his Ph.D. degree in organic chemistry from Nankai University under the guidance of Professor Weidong Li. In 2013, he began his career at Qingdao University of Science and Technology. In 2019, he joined Professor Jieping Zhu's group as a postdoctoral fellow in EPFL, Switzerland. Currently, he is an associate professor at Qingdao University of Science and Technology and focuses on developing new electrochemical methodologies for the synthesis of functionalized molecules.

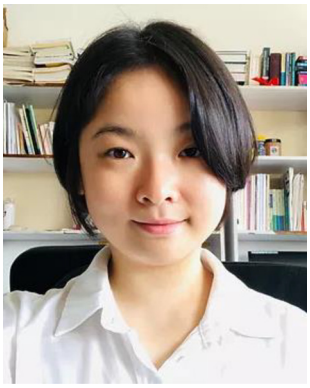

Tianwei Duan

Dr Tianwei Duan is currently a postdoctoral research fellow in the Advanced Semiconductor Laboratory (ΣLab) at Hong Kong Baptist University, funded by the prestigious Hong Kong RGC Postdoctoral Fellowship Scheme. She received her B.S. (2012) and M.S. (2015) degrees from Tongji University and her Ph.D. (2021) degree in chemistry from Shanghai Jiao Tong University. Her research currently focuses on chiral semiconductors and emerging electronics.

Experimental and theoretical studies have revealed that the t value of the ABX_3 perovskite generally ranges between 0.8 and 1. When the t value deviates from 1, other low-symmetry structures or nonperovskite phases are usually generated.[39] Taking $CsPbI_3$ as an example, γ-$CsPbI_3$ (perovskite phase) can be transformed into δ-$CsPbI_3$ (nonperovskite phase) at room temperature (RT) due to the low t value of 0.81.[40,41] To obtain stable all-inorganic perovskites, the radius of divalent cations (B-site) should be less than that of lead so that the t value can approach 1. Several potential candidates for divalent cations inculde Ge^{2+}, Sn^{2+}, Cu^{2+}, Ni^{2+}, Co^{2+}, Fe^{2+}, Mn^{2+}, *etc*. Sn and Ge are regarded as the key Pb substitutes due to their similar electronic structures. According to eqn (1), the value of t will increase gradually towards the perfect cubic phase when Sn or Ge is introduced to replace Pb entirely or partially.[38]

Electronic band structure

The valence band maximum (VBM) of the ABX_3 perovskite is mainly determined by the formation of antibonding orbitals through hybridization between the B cation's s orbitals and the X anion's p orbitals, while the conduction band minimum (CBM) depends on the p orbitals of both the B cation and the X anion. The well-studied inorganic perovskite of $CsPbI_3$ exhibits a bandgap of 1.73 eV, which exceeds the ideal-bandgap region (1.2–1.4 eV) according to the Shockley–Queisser limit.[42] Replacing Pb with Sn or Ge with a smaller atom radius can significantly reduce the bandgap and increase the energy conversion efficiency. The experimentally derived bandgaps of $CsSnI_3$ and $CsGeI_3$ are 1.3 eV (ref. 43 and 44) and 1.6 eV, respectively.[45] In addition, it is possible to further optimize the electronic band structures in $CsSnI_3$ and $CsGeI_3$. Transition metals with unfilled d orbitals can hybridize with the p orbitals of X anions, leading to an increase in the VBM and bandgap narrowing. For example, the indirect bandgaps of $CsSnI_3$ can dramatically decrease when the replacement of partial Sn^{2+} ions with small-sized Cu^{2+} is over half.[46]

The bandgaps of inorganic perovskites can also be effectively changed by the alloying strategy, which entails adjusting the mixing proportion of different ions at either B or X sites. For B-site alloying, benefited from the bowing effect, it is possible to form perovskite B-site alloys with even lower bandgaps than their pure-composition counterparts. This phenomenon has been exemplified by Pb–Sn alloying perovskites.[47,48] Taking $CsPb_xSn_{1-x}Br_3$ as an example, the bandgaps for $CsPbBr_3$ and $CsSnBr_3$ are 2.37 eV and 1.86 eV, respectively. While the bandgap change in the alloying perovskite is nonlinear in x with a bowing parameter of 0.9 eV, a low Pb content ($x \sim 0.3$) in the alloying perovskite shows a much narrowed bandgap of 1.82 eV. Density functional theory (DFT) calculations reveal that this can be related to the crystal structure transformation. It is found that the orthorhombic phase of $CsPbBr_3$ is in a tilted configuration. With the introduction of Sn^{2+} with a smaller ion radius, a lattice distortion is reduced, and the B–X–B bond angle gradually expands to 180°.[49] For X-sitealloying in perovskites, anions exhibit increasing ionization energy and electron affinity from I^-, Br^- to Cl^-, leading to a decrease in the B–X distance, and subsequently causing a large downward shift of the VBM.[50,51] Apart from the bandgap factor, the stability issues resulted from anion mixing should also be considered. On one hand, the replacement of I^- ions with Br^- ions in perovskites can stabilize the perovskite phase. On the other hand, mixed-anion perovskites undergo phase segregation under light stimulus and the migration of halide ions can lead to the formation of in-gap trap states.[52] For the A-site alloying in perovskites, it is generally considered that the A-site cations do not directly affect the bandgap, they can still impact the electronic band structures by possibly influencing the B–X bond length.[53]

All-inorganic PSC devices based on mixed group IVA cations

All-inorganic perovskites based on mixed group IVA cations possess several advantages in terms of phase stability and bandgaps. This section focuses mainly on the three types of

Zhongmin Zhou

Dr Zhongmin Zhou is currently a professor at Qingdao University of Science and Technology. He received his Ph.D. degree from the Institute of Chemistry, Chinese Academy of Sciences (CAS) in 2014 and then conducted postdoctoral research at CAS – Qingdao Institute of Bioenergy and Bioprocess Technology, National Institute of Materials Science (NIMS), and The University of Tokyo. His research interest is in functional materials and devices.

Yuanyuan Zhou

*Dr Yuanyuan (Alvin) Zhou is currently Principal Investigator of the Advanced Semiconductor Laboratory (ΣLab) and Assistant Professor in the Department of Physics at Hong Kong Baptist University. He earned his Ph.D. in Engineering from Brown University in 2016. ΣLab (**https://www.alvinyzhou.com**) focuses on innovating semiconductor technologies for sustainable and smart society* via *transdisciplinary approaches.*

perovskite compositions: $CsPb_xSn_{1-x}I_yBr_{3-y}$, $CsPb_xGe_{1-x}I_yBr_{3-y}$, and $CsSn_xGe_{1-x}I_yBr_{3-y}$. Among these, $CsPb_xSn_{1-x}I_yBr_{3-y}$ is the most extensively studied composition due to the stability of Pb^{2+} in air. Accordingly, we summarize the performance improvement of all-inorganic $CsPb_xSn_{1-x}I_yBr_{3-y}$ perovskites from the aspects of compositional engineering, morphology engineering, and additive engineering. Research studies on Sn and Ge-related perovskite compositions are still in their early phases, and only a handful of related studies have been reported, which will be reviewed in details. Furthermore, we will also discuss the research progress on perovskite nanomaterials of the above compositions.

$CsPb_xSn_{1-x}I_yBr_{3-y}$ perovskite

Compositional engineering. Although lead-based all-inorganic PSCs exhibit excellent photoelectric properties, their stability at RT is inferior. Partial substitution of Pb^{2+} ions with smaller metal ions like Sn^{2+} or Ge^{2+}, as well as partial replacement of I^- ions with smaller Br^- ions, are considered the most feasible method to adjust the tolerance factor (t). This can improve the stability of the photoactive phase at RT, increase the formation energy of point defects, and suppress the generation of point defects.[54–57]

For example, Lee *et al.* fabricated an all-inorganic Sn-rich perovskite material, $CsPb_{0.4}Sn_{0.6}I_{2.4}Br_{0.6}$, with an excellent bandgap of 1.35 eV.[58] The authors investigated the t value and defect formation energy of perovskite materials with different contents of Sn and Pb through DFT simulation. As the content of Sn^{2+} increased to 100%, the t value increased from 0.807 to 0.875, but the defect formation energy reached the lowest point when the content of Sn^{2+} decreased to 50%. Moreover, the authors investigated the humidity stability of perovskite samples with different Sn^{2+} contents by monitoring the evolution of X-ray diffraction (XRD) patterns, photoluminescence (PL) spectra, and ultraviolet–visible (UV-vis) spectra upon storage in a high-humidity environment for 1 h to several days. The results showed that $CsPb_{0.4}Sn_{0.6}I_3$ has an even higher humidity stability compared to $CsPbI_3$. Subsequently, the authors introduced Br^- into $CsPb_{0.4}Sn_{0.6}I_3$to prepare a perovskite material of $CsPb_{0.4}Sn_{0.6}I_{2.4}Br_{0.6}$, which shows a further improved structural stability together with a high tolerance to the thermal degradation caused by heat-induced strain.

Liang *et al.* prepared an all-inorganic Sn–Pb hybrid perovskite of $CsPb_{0.9}Sn_{0.1}IBr_2$ in the ambient air,[59] and revealed it has a narrow bandgap of 1.79 eV. $CsPb_{0.9}Sn_{0.1}IBr_2$-based PSCs show a high open-circuit voltage (V_{OC}) of 1.26 V and a PCE of 11.33%. In their devices, a layer of carbon electrode replaced the hole transport material (HTM) layer and the gold electrode, which not only avoided the use of expensive noble metal electrodes but also eliminated unstable organic components in the device. As a result, the encapsulated device exhibited negligible degradation after 3 months of storage at RT and remained operational after 2 weeks of heating at 100 °C. Even when exposed to the ambient air of 50–60% relative humidity (RH) for 50 h at RT, an unencapsulated device still maintains 85% of its initial PCE, demonstrating an improved moisture tolereance.

Morphology engineering. The performance of PSCs is closely related to the morphology of the perovskite films. Since the nucleation and grain growth processes of the perovskite generally follow the Volmer–Weber mode,[60] a high-quality perovskite thin film refers to a polycrystalline thin film with dense, uniform, pinhole-free, large grain size, and low grain boundary density characteristics. A high density is the key to preventing short circuits and reducing leakage current. Increasing the grain size of the perovskite and reducing the grain boundary can effectively lower the defect density and restrain the non-radiative combination loss.[61] In addition, perovskite films with higher crystal quality possess flatter surfaces, which can fully contact the carrier transport layer, effectively reduce the interface defects, enhance carrier extraction efficiency at the interface, and thus improve the device performance.

The quality of the perovskite films depends mainly on the preparation method. There are two commonly used fabrication methods, including one-step spin-coating and two-step deposition. However, it is difficult to control the stoichiometry of perovskite films with relatively complex compositions using two-step sequential deposition,[59] making one-step deposition the preferred method for synthesizing inorganic perovskites with mixed group IVA cations. Li *et al.* used a one-step antisolvent method to prepare $CsPb_{1-x}Sn_xIBr_2$ perovskite films.[62] With an increase in the Sn content, there is a red shift in the UV-vis absorption spectrum of $CsPb_{1-x}Sn_xIBr_2$, indicating a smaller bandgap with a higher Sn content (Fig. 2a). The reduced bandgap of perovskite materials can absorb more photons and achieve a higher photocurrent under illumination. As the Sn content increases from 0 to 1, results based on scanning electron microscopy (SEM)show a clear effect of alloying on the quality of perovskite films. When the Sn content reaches 0.25, a perovskite film with a compact polycrystalline grain morphology is obtained. However, further increasing the Sn content can lead to an over-acceleration of the crystallization rate, causing an uncontrolled film quality. As a result, the number of pinholes in the perovskite film increases, and the

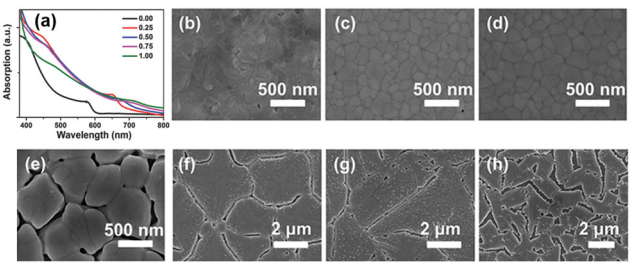

Fig. 2 (a) UV-vis absorption spectra of $CsPb_{1-x}Sn_xIBr_2$ with varing x Reproduced from ref. 63 with permission from Wiley-VCH. Copyright 2018. Top-view SEM images of $CsPb_{1-x}Sn_xI_3$ films with (b) x = 0, (c) x = 0.25, (d) x = 0.30, (e) x = 0.50, (f) x = 0.75, (g) x = 0.88, and (h) x = 1.00. Reproduced from ref. 64 with permission from the American Chemical Society. Copyright 2020.

surface becomes rough, leading to undesired carrier recombination and transport properties. Yang *et al.* found that the grain size of the perovskite films could reach the micrometer level with an increase in the Sn content.[63] A similar phenomenon about the larger crystal size by increasing the Sn content can also be observed in $CsPb_{1-x}Sn_xI_3$-based perovskites (Fig. 2b–h). Similar to the earlier results,[61] in the study by Yang *et al.*, both PL and UV-vis spectra exhibit clear red shifts with an increase in the Sn content, and the short-circuit current density (J_{SC}) increases due to the decreased bandgap. The devices with a structure of indium-doped tin oxide (ITO)/poly (3,4-ethylenedioxythiophene)poly(styrenesulfonate) (PEDOT:PSS)/$CsSn_{0.3}Pb_{0.7}I_3$/[6,6]-phenyl-C_{61}-butyric acid methyl ester (PCBM)/bathocuproine (BCP)/Ag exhibited a companion PCE of 9.4%. Besides, the authors also successfully fabricated HTM-free inverted devices based on $CsSn_{0.3}Pb_{0.7}I_3$, which demonstrate a promising PCE of 7.6%.

Hu *et al.* employed a one-step spin-coating method without using an anti-solvent to prepare uniform $CsPb_{0.6}Sn_{0.4}I_3$ perovskite films with good structural stability and high Sn^{2+} stability.[64] However, these films remain vulnerable to water and show limited stability in the ambient air. To further improve the environmental stability, the authors first introduced a SnF_2·3FACl additive into the $CsPb_{0.6}Sn_{0.4}I_3$ precursor solution to functionalize the grain boundaries of perovskite thin films. Then, an organic salt, (aminomethyl) piperidinium diiodide (4AMP)I_2, was used on the surface of $CsPb_{0.6}Sn_{0.4}I_3$ to form a hydrophobic blocking layer and also to passivate the defects of perovskite thin films. Fig. 3a–c show the SEM images of the pristine perovskite film, the SnF_2·3FACl incorperated perovskite film, and the SnF_2·3FACl and (4AMP)I_2 treated perovskite film, which are denoted as N-$CsPb_{0.6}Sn_{0.4}I_3$, G-$CsPb_{0.6}Sn_{0.4}I_3$, and G-S-$CsPb_{0.6}Sn_{0.4}I_3$, respectively. The introduction of SnF_2·3FACl can increase the grain size and reduce defect density, and the resulting UV-vis spectroscopy also shows improved absorption characteristics. The trap density of the perovskite films was estimated through space-current-limited-charge (SCLC) measurements.[65,66] As shown in Fig. 3d, the trap-filled limited voltages (V_{TFL}) are 1.11 V, 0.61 V, and 0.34 V for $CsPb_{0.6}Sn_{0.4}I_3$, G-$CsPb_{0.6}Sn_{0.4}I_3$, and G-S-$CsPb_{0.6}Sn_{0.4}I_3$, respectively. The estimated trap densities for $CsPb_{0.6}Sn_{0.4}I_3$, G-$CsPb_{0.6}Sn_{0.4}I_3$, and G-S-$CsPb_{0.6}Sn_{0.4}I_3$ are 5.50×10^{16}, 3.02×10^{16}, and 1.68×10^{16} cm^{-3}, respectively. The device structure of fluorine-doped tin oxide (FTO)/NiO_x/perovskite/PCBM/BCP/Ag was exploited. The devices based on $CsPb_{0.6}Sn_{0.4}I_3$, G-$CsPb_{0.6}Sn_{0.4}I_3$, and G-S-$CsPb_{0.6}Sn_{0.4}I_3$ show PCEs of 0.92%, 5.68% and 11.28% (Fig. 3e), respectively. In terms of the continuous operation lifetime of the devices under one-sun illumination, after 1000 h of continuous operation, the device still retained 77% of its initial PCE.

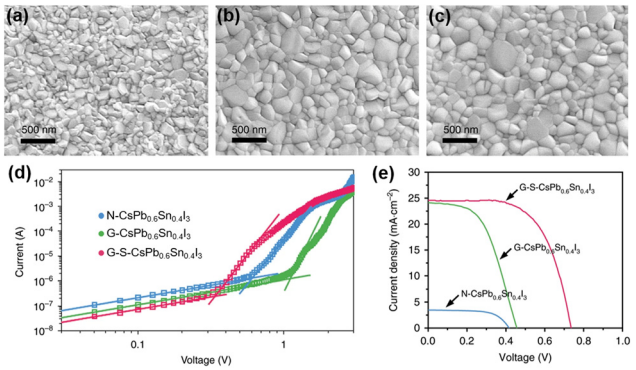

Fig. 3 Top-view SEM images of (a) N-$CsPb_{0.6}Sn_{0.4}I_3$, (b) G-$CsPb_{0.6}Sn_{0.4}I_3$, and (c) G-S-$CsPb_{0.6}Sn_{0.4}I_3$, (d) Dark *I*–*V* curves of N-$CsPb_{0.6}Sn_{0.4}I_3$, G-$CsPb_{0.6}Sn_{0.4}I_3$, and G-S-$CsPb_{0.6}Sn_{0.4}I_3$ films, and (e) *J*–*V* curves of N-$CsPb_{0.6}Sn_{0.4}I_3$, G-$CsPb_{0.6}Sn_{0.4}I_3$, and G-S-$CsPb_{0.6}Sn_{0.4}I_3$ devices. N-$CsPb_{0.6}Sn_{0.4}I_3$, G-$CsPb_{0.6}Sn_{0.4}I_3$, and G-S-$CsPb_{0.6}Sn_{0.4}I_3$ refer to $CsPb_{0.6}Sn_{0.4}I_3$ films without additional treatment, with SnF_2·3FACl grain boundary treatment, and with both SnF_2·3FACl and (4AMP)I_2 treatments, respectively. Reproduced from ref. 64 with permission from Springer Nature. Copyright 2020.

Additive engineering. The phase stability, defect density, and phase segregation of inorganic perovskites can be effectively regulated by introducing additives.[67] Although Sn element doping in $CsPbX_3$ results in all-inorganic alloy perovskites with better bandgap and stress release, it also brings "notorious" p-type self-doping due to the oxidation of Sn^{2+} to Sn^{4+}. In this section, we review those interesting studies harnessing the functions of various additives to effectively retard the oxidation of Sn^{2+} to Sn^{4+} and improve the performance of devices.

Chen *et al.* employed a one-step anti-solvent method for synthesizing a group of $CsPb_{1-x}Sn_xI_2Br$ perovskites at a low annealing temperature (60 °C).[68] As shown in Fig. 4a, $CsPb_{0.55}Sn_{0.45}I_2Br$ can exhibit the best thermal stability as compared to $CsPbI_2Br$ and $MAPbI_3$ perovskite films under continuousannealing at 150 °C in an N_2 glovebox. Then, Chen et al used CsCl and $PbSO_4$ as additives and passivators, respectively, to improve the performance and stability of $CsPb_{1-x}Sn_xI_2Br$-based devices. The Cl^- ions in CsCl help enlarge perovskite grains and also possibly fill iodine vacancies (V_I), while $PbSO_4$ acts as a passivation layer, which not only interacts with the uncoordinated Pb^{2+} to reduce defect-assisted carrier recombination but also forms a dense and hydrophobiccoating on the surface of the perovskite layer to prevent the intrusion of external oxygen and water as well as the migration of I^-. The $CsPb_{0.55}Sn_{0.45}I_2Br$–CsCl–$PbSO_4$-based devices with a stacking structure of ITO/PEDOT:PSS/perovskite/$PC_{61}BM$/Ag show the highest PCE of 10.39% with negligible hysteresis. Additionally, the $CsPb_{0.55}Sn_{0.45}I_2Br$–CsCl–$PbSO_4$-based device show outstanding shelf stability with 92.5% retention of initial PCE after 2000 h in an N_2-filled glovebox, as compared to 72.66% for the $CsPb_{0.55}Sn_{0.45}I_2Br$-based devices (Fig. 4b and c). Fig. 4d shows the operational stability (maximum-power-point tracking, MPPT) of unencapsulated devices with $CsPb_{0.55}Sn_{0.45}I_2Br$, $CsPb_{0.55}Sn_{0.45}I_2Br$–CsCl and $CsPb_{0.55}Sn_{0.45}I_2Br$–CsCl–$PbSO_4$ as the photoactive layers.

The $CsPb_{0.55}Sn_{0.45}I_2Br$–CsCl–$PbSO_4$-based device retained 80% of its initial PCE after 300 h of continuous illumination, while the PCEs of $CsPb_{0.55}Sn_{0.45}I_2Br$- and $CsPb_{0.55}Sn_{0.45}I_2Br$–

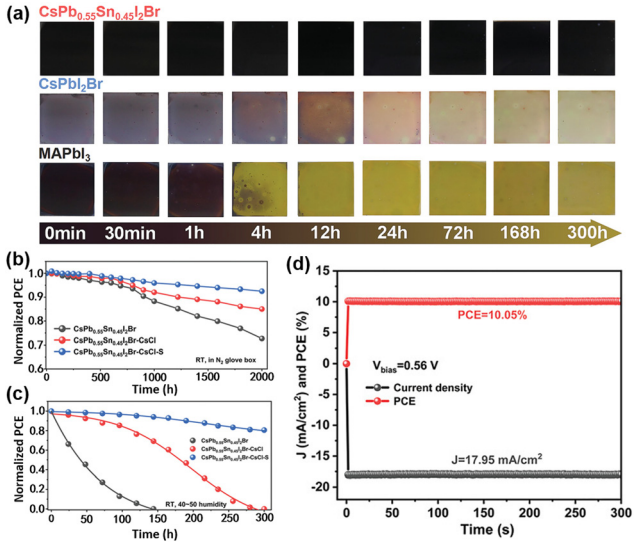

Fig. 4 (a) Photographs of $CsPb_{0.55}Sn_{0.45}I_2Br$, $CsPbI_2Br$ and $MAPbI_3$ perovskite films under iso-thermal annealing (150 °C) in an N_2-filled glove box. The long-term normalized PCE of PSCs (b) in an N_2-filled glovebox and (c) in the ambient air (40–50% RH). (d) MPPT of a $CsPb_{0.55}Sn_{0.45}I_2Br$-CsCl-S-based device. Reproduced from ref. 68 with permission from Wiley-VCH. Copyright 2021.

CsCl-based devices decreased to zero after 120 h and 280 h of continuous illumination, respectively.

A seed-assisted growth (SAG) method was used to fabricate a series of high-quality $CsPb_{1-x}Sn_xIBr_2$ films.[69] To inhibit the oxidation of Sn^{2+} to Sn^{4+}, reduce the trap density and improve the perovskite film morphology, zinc oxalate (ZnO_x) was introduced into the perovskite precursor solution as an additive. Fig. 5a illustrates the photographs of perovskite solutions with/without ZnO_x exposure to air. The color of the ZnO_x-treated solution remained unchanged upon storage. In contrast, the control perovskite precursor solution turned reddish-brown from yellow after 72 h, indicating the inhibition of Sn^{2+} to Sn^{4+} due to the addition of ZnO_x. Moreover, the oxidation product of the oxalate anion was CO_2, avoiding the introduction of impurities into the perovskite film. Oxalate is an excellent ligand and can interact strongly with uncoordinated metal ions, as characterized by the Fourier-transform infrared (FTIR) spectra as shown in Fig. 5b. The coordination interaction can retard the crystallization of the perovskite, leading to a high-quality film. As shown in Fig. 5c, there are some pinholes and voids in the control film, while the ZnO_x-treated film shows a full coverage with larger grains. Additionally, Zn^{2+} cations can refill Sn vacancies (V_{Sn}) and lead to vacancies (V_{Pb}) in the perovskite films. Besides, the introduction of ZnO_x can reduce charge recombination and help to improve the device efficiency. As a result, the ZnO_x-treated champion device shows a companion PCE of 14.1% with a hysteresis H-index of 4.2% as compared to the 12.9% PCE with a hysteresis H-index of 6.2% for the control device. The ZnO_x-treated device also exhibit better long-term shelf lifetime and thermal stability than the control device.

SnF_2 has been extensively used as an additive in Sn-based perovskites to retard the oxidation of Sn^{2+} to Sn^{4+}.[70–72] However, its uneven dispersion in the film would lead to the phase separation of the perovskite, resulting in a low-quality film.[73] To address this issue, Ban *et al.* introduced tea polyphenol (TP) into the perovskite precursor solution to retard the oxidation of Sn^{2+} and modulate perovskite crystallization dynamics.[74] Fig. 6a shows the color evolution of the perovskite precursor solutions with/without TP (0.5 wt%) in air. The control film (without TP) exhibited a noticeable color variance from yellow to dark red (a typical color of Sn^{4+} solution) after 72 h of exposure to air, indicating the oxidation of Sn^{2+}. In contrast, the TP-treated film showed no color change after the same period, indicateing that TP can retard the oxidation of Sn^{2+}. In addition to slowing down the oxidation rate of Sn^{2+} to Sn^{4+}, the coordination between TP and the perovskite, confirmed by FTIR characterization, can promote the crystallization of the perovskite, resulting in a uniform and dense high-quality film (Fig. 6b). As a result, the device with a structure of FTO/c-TiO_2/$CsPb_{0.5}Sn_{0.5}I_2Br$/Al_2O_3/NiO/carbon exhibits an improved PCE of 8.1% with the introduction of TP compared

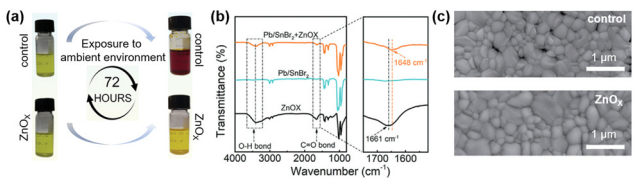

Fig. 5 (a) Photographs confirming oxalate retarding the Sn^{2+} oxidation. (b) FTIR spectra and the characteristic regions of pure ZnO_x, $Pb/SnBr_2$, and $Pb/SnBr_2$ + ZnO_x in DMSO. (c) Top-view SEM images of $CsPb_{0.7}Sn_{0.3}IBr_2$ thin films with and without ZnO_x. Reproduced from ref. 67 with permission from Wiley-VCH, copyright 2022.

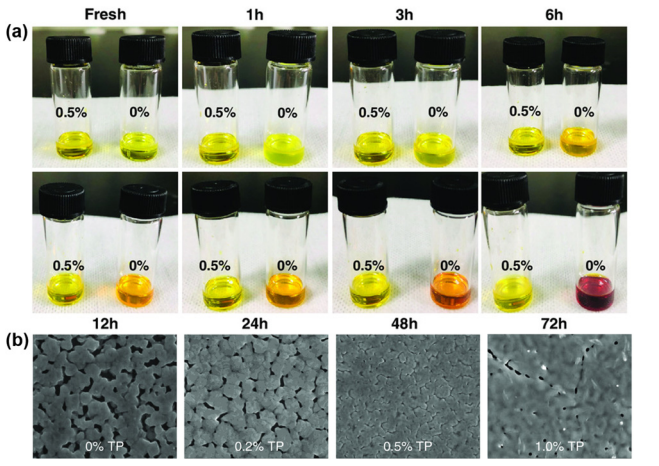

Fig. 6 (a) Photographs of $CsPb_{0.5}Sn_{0.5}I_2Br$ precursor solutions with and without TP (0.5%). (b) Top-view SEM images of $CsPb_{0.5}Sn_{0.5}I_2Br$ thin films with varing TP contents. Reproduced from ref. 74 with permission from Wiley-VCH. Copyright 2020.

with that of 4.98% for a control device. In addition, the TP-treated device shows an improved shelf lifetime, maintaining 94% efficiency after 60 days of storage in a glovebox.

Nano-engineering. Nano-engineering is another effective strategy to obtain perovskite materials with unique opto-electronic and chemical properties, which is attributed to the quantum effects and intra-crystal strains. The application of $CsPbI_3$ quantum dots (QDs) in PSCs has been previously reported,[75,76] and the bandgap of the perovskite can be adjusted by controlling the size of the generated QDs. $CsPbI_3$ has a large bandgap (1.73 eV) for single-junction solar cells, and the bandgap of $CsPbI_3$ QDs becomes larger due to the quantum confinement effect. To reduce the bandgap of perovskite QDs, Liu *et al.* synthesized Sn–Pb alloyed perovskite ($CsPb_xSn_{1-x}I_3$) QDs.[77] Adjusting the ratio of Sn/Pb in the perovskite precursor solution exerts negligible effects on the final QDs' size, but both time-resolved infrared spectroscopy and Urbach energy studies indicate that the density of defect states in QDs becomes larger with an increase in the Sn content in the quantum dots. This is because Sn^{2+} can be easily oxidized to Sn^{4+} and generates V_{Sn}, acting as nonradiative recombination centers. However, since the Sn^{2+} ionic radius is smaller than that of Pb^{2+}, the addition of Sn is beneficial for maintaining the perovskite crystal structure from the persepctive of the tolerance factor *t*. Therefore, it is claimed that the alloyed QDs exhibit excellent overall stability in both solution and ambient air.

$CsPb_xSn_{1-x}I_3$ nanowires (NWs) were also synthesized by a two-step synthesis method,[78] and their structure and phase transition properties were investigated by XRD (Fig. 7a). A series of XRD patterns of $CsPb_xSn_{1-x}I_3$ indicate that there are no characteristic peaks of the starting material, and the characteristic peaks of the yellow (Y-) phase are similar to those of the nonperovskite phase of $CsPbI_3$. After annealing, the generated black-γ (B-γ) phase (photoactive phase) perovskite NWs were obtained (Fig. 7b). The phase transition temperature of NWs with different Sn doping ratios was investigated, showing the growth trend with an increase in the lead content. Moreover, the bandgap of $CsPb_xSn_{1-x}I_3$ NWs decreases with an increasein the Sn content. Electrical conductivity measurements showed that both Y-phase and B-phase NWs had higher conductivity with increasing Sn content, consistent with previous findings on the increased hole density in perovskites due to Sn vacancies.[79] Moreover, the Seebeck coefficient measurement suggests that the $CsPb_xSn_{1-x}I_3$ NWs are p-type semiconductors.

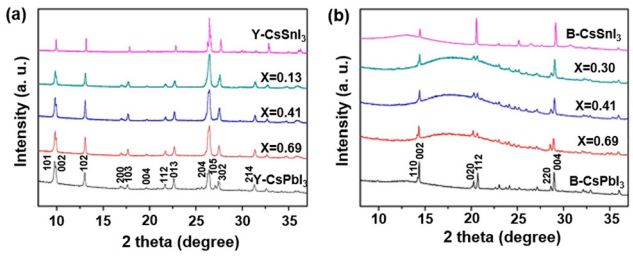

Fig. 7 XRD patterns of (a) Y-phase $CsPb_xSn_{1-x}I_3$ NWs and (b) B-γ phase $CsPb_xSn_{1-x}I_3$ NWs. Reproduced from ref. 78 with permission from the American Chemical Society. Copyright 2018.

$CsPb_xGe_{1-x}I_yBr_{3-y}$ perovskite

Ge is a metal-like element in nature with relatively low toxicity compared to Pb. Thus, B-site alloying has also been explored for Pb–Ge based perovskites. Yang *et al.* introduced Ge into $CsPbI_2Br$ to fabricate $CsPb_{1-x}Ge_xI_2Br$ (x = 0, 0.1, 0.2, 0.3) perovskites at a low temperature (160 °C) in air with 50–60% RH.[80] After an optimumaddition of Ge, the $CsPb_{0.8}Ge_{0.2}I_2Br$ perovskite film maintains the cubic perovskite phase under 50–60% RH for 120 h, while the cubic phase of the control all-inorganic perovskite film changes to the nonperovskite phase rapidly within 10 min. The $CsPb_{0.8}Ge_{0.2}I_2Br$-based devices showed a champion PCE of 10.8% compared to that of 5.3% for the $CsPbI_2Br$-based devices, which mainly resulted from the lower carrier recombination rate with the incorporation of Ge. In addition, the humidity stability of the device was also tested, and the performance of the device did not decrease after exposure to air with 50–60% RH for more than 7 h. For comparison, a rapid PCE decrease within 2 h is seen for the control $CsPbI_2Br$-based device (Fig. 8).

Previous studies have shown that Ge is a potential element to replace Pb in Pb-less or even Pb-free perovskites. Because Cu^{2+} and Ge^{2+} possess the same ionic radius, Wang *et al.* used density functional theory (DFT) to study the effect of Ge/Cu binary co-doping on $CsPbBr_3$-based perovskites.[81] The authors examined the relationship between the lattice volume of $CsPb_{1-x}Ge_xBr_3$ and $CsPb_{1-x}Cu_xBr_3$ (Fig. 9a). The higher strength of Cu–Br bonds in $CsPb_{1-x}Cu_xBr_3$ results in changes in bond lengths and bond angles, improving the charge trans-

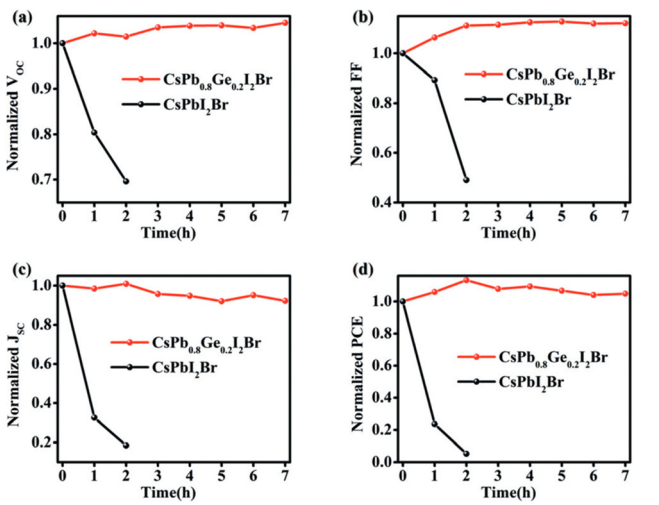

Fig. 8 Stability tests of $CsPb_{0.8}Ge_{0.2}I_2Br$ and $CsPbI_2Br$ PSCs upon the storage in the ambient atmosphere (50--60 % RH): (a) V_{OC}, (b) FF, (c) J_{SC}, and (d) PCE. Reproduced from ref. 80 with permission from Wiley-VCH. Copyright 2018.

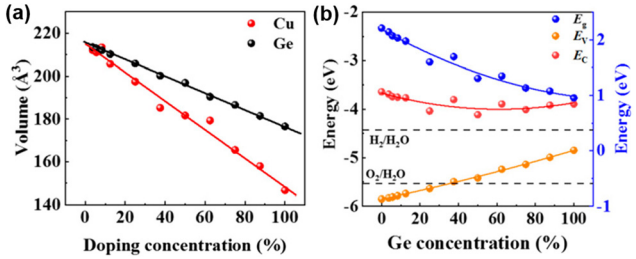

Fig. 9 (a) Normalized volumes of Ge- and Cu-doped bulk $CsPbBr_3$. (b) Bandgap coupled to the energies of the VBM and the CBM for $CsPb_{1-x}GexBr_3$. Reproduced from ref. 81 with permission from the American Chemical Society. Copyright 2021.

port properties of perovskites. When the content of Ge is greater than 27.5%, with the increase of Ge doping concentration, although the light absorption range is broadened, the CBM and VBM of $CsPb_{1-x}Ge_xBr_3$ are larger than the oxidation potentials of H_2O/H_2 and H_2O/O_2, respectively, meaning that Ge^{2+} is easily oxidized to Ge^{4+} (Fig. 9b). The ability of Cu to redistribute charges allows it to extract electrons from the bulk phase of the perovskite. The formation energy of Cu on the surface is lower than that in the bulk phase due to the tendency of V_{pb} to appear on the perovskite surface. The Cu doping on the surface effectively inhibits the erosion of the perovskite by moisture. This moisture resistance can be achieved by increasing the doping amount of Cu, and more Cu/Ge doping not only reduces the toxic Pb content but also improves the light absorption in the visible light wavelength range.

$CsSn_xGe_{1-x}I_yBr_{3-y}$ perovskite

Since Ge replaces part of Sn in $CsSnI_3$, the t value of the perovskite reaches 0.94, leading to a high stability of the lattice structure. Chen *et al.* used the one-step vapor-processing method to fabricate Pb-free $CsSn_{0.5}Ge_{0.5}I_3$.[82] Moreover, the extremely high oxidation activity of Ge(II) can form an ultrathin uniform natural oxide surface passivation layer on the surface of the perovskite film after exposing to an ambient atmosphere for 30 s, which is GeO_2 as indicated by X-ray photoelectron spectroscopy (XPS) analysis (Fig. 10). The as-obtained perovskite powders remain phase-stable whether directly exposed to high-humidity air or subjected to continuous one-sun illumination. $CsSn_{0.5}Ge_{0.5}I_3$-based devices with a configuration of FTO/PCBM/$CsSn_{0.5}Ge_{0.5}I_3$/spiro/Au show a champion PCE of 7.11%. Moreover, after 500 h of continuous operation under a nitrogen atmosphere, the unencapsulated device can maintain 92% of its initial PCE. Subsequently, several research groups have evaluated tin–germanium hybrid all-inorganic perovskites from the perspectives of the crystal structure, optoelectronic properties, and defect properties based on first-principles calculations.[83–86] Through simulation calculations, it is found that the alloy with Ge/Sn = 1 shows the best optical absorption and benign defects. Ge doping has a remarkable effect on

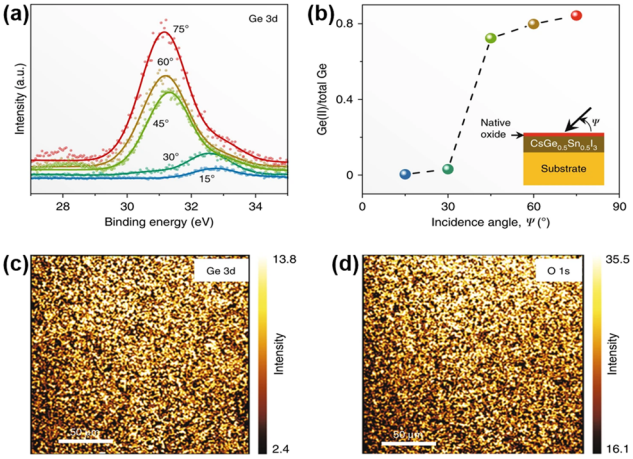

Fig. 10 (a) Ge 3d XPS spectra at different incidence angles in a vapor-deposited $CsSn_{0.5}Ge_{0.5}I_3$ film. (b) The corresponding plot of the Ge(II) fraction *vs.* the incidence angle. (c) and (d) XPS maps of Ge 3d (33 eV) and O 1s (532 eV). Reproduced from ref. 82 with permission from Springer Nature. Copyright 2020.

eliminating deep defects, which provides new insights into the evolution and regulation of defect properties.

Liu *et al.* first fabricated all-inorganic Sn–Ge alloy perovskite nanocrystals (PNCs) using the hot injection method.[86] Compared with Sn-based PNCs, these Sn–Ge-based PNCs exhibited significantly improved optical properties, and the stability of perovskites was also effectively enhanced. The partial substitution of Sn atoms by Ge in PNCs can effectively fill the high density of V_{Sn} and reduce surface traps, thereby prolonging the exciton lifetime and improving the photoluminescence quantum yields (PLQYs). Although the adding amounts of SnI_2 and GeI_2 are equal in the synthesis of PNCs, the results indicated that the substitution ratio of Ge does not reach 50%. Therefore, the authors determine the final light-absorbing layer component as $CsSn_{0.6}Ge_{0.4}I_3$. In both UV-vis and PL results, an obvious blue-shift is observed, and the PL of $CsSn_{0.6}Ge_{0.4}I_3$ had a sub-peak at 725 nm in addition to the main peak at 780 nm (Fig. 11a). The authors speculated that there are a small amount of carbon nanorods in addition to PNCs. Time-resolved photoluminescence (TRPL) test results show that the carrier lifetime of $CsSn_{0.6}Ge_{0.4}I_3$ is longer than

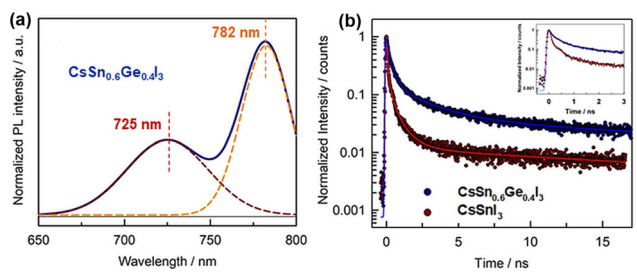

Fig. 11 (a) Steady-state PL spectra of $CsSn_{0.6}Ge_{0.4}I_3$ NCs. (b) TRPL spectra of $CsSn_{0.6}Ge_{0.4}I_3$ and $CsSnI_3$. Reproduced from ref. 86 with permission from Wiley-VCH, copyright 2020.

Table 1 Device performance parameters and stability of all-inorganic perovskites featuring mixed group IVA cations

Devices structure	V_{OC} (V)	J_{SC} (mA cm^{-2})	FF	PCE (%)	Stability (conditions)	Ref.
FTO/c-TiO_2/m-TiO_2/$CsPb_{0.9}Sn_{0.1}IBr_2$/carbon	1.26	14.30	0.63	11.33	>300 h (encapsulated, 100 °C)	55
FTO/c-TiO_2/m-TiO_2/$CsPb_{0.4}Sn_{0.6}IBr_2$ QDs/spiro/Au	0.63	10.13	0.46	2.9	>1 month (30%–40% RH, RT)	75
ITO/SnO_2/C_{60}/$CsPb_{0.75}Sn_{0.25}IBr_2$/spiro/Au	1.21	12.57	0.76	11.53	Maintaining 80% of its initial PCE after storing for 1000 h (50–60% RH encapsulated, RT)	58
ITO/PEDOT/PSS/$CsPb_{0.7}Sn_{0.3}IBr_2$/PCBM/(BCP)/Ag	0.64	20.96	0.7	9.41	Maintaining 97% of its initial PCE after storing for 6 months and maintaining 94.86% of its initial PCE after 186 h continuous illumination (in a nitrogen-filled glovebox)	63
FTO/c-TiO_2/m-TiO_2/$CsPb_{0.5}Sn_{0.5}I_2Br$/Al_2O_3/NiO/carbon	0.61	20.1	0.65	8.1	Maintaining 94% of its initial PCE after storing for 60 days and maintaining 90.1% of its initial PCE for 200 h MPPT (in a nitrogen-filled glovebox)	72
FTO/NiO_x/$CsPb_{0.6}Sn_{0.4}I_3$/PCBM/Ag	0.774	25.87	0.67	13.37	No PCE degradation after storing for 2800 h (dry, N_2, RT)	64
ITO/SnO_2/$CsPb_{0.7}Sn_{0.3}IBr_2$/PCBM/Ag	1.18	15.5	0.77	14.1	Maintaining 75% of its initial PCE after storing for 10 days (in air, RT)	67
ITO/PEDOT:PSS/$CsPb_{0.55}Sn_{0.45}I_2Br$/sulfate/PCB61M/BCP/Ag	0.7	20.57	0.72	10.39	Maintaining 80% of its initial PCE for 300 h MPPT (in air, 40–50% RH)	66
FTO/PCBM/$CsSn_{0.5}Ge_{0.5}I_3$/spiro/Au	0.63	18.61	0.61	7.11	Maintaining 92% of its initial PCE for 500 h continuous operation (N_2, 45 °C)	80
FTO/c-TiO_2/$CsSn_{0.6}Ge_{0.4}I_3$ NCs/spiro/MoO_3/Au	0.65	11.8	0.64	4.9		84
FTO/SnO_2/$CsPb_{0.8}Ge_{0.2}I_2Br$/P3HT/spiro/Au	1.27	12.15	0.7	10.8	No PCE degradation after storing for 7 h (in air, 50–60 RH)	78

that of $CsSnI_3$, indicating that Ge incorperation leads to a lower defect concentration. This supports the hypothesis that Ge^{2+} with a smaller ionic radius easily fills the V_{Sn}, reducing the density of defects (Fig. 11b). Conventional devices with a structure of FTO/c-TiO_2/$CsSn_{0.6}Ge_{0.4}I_3$/spiro-OMeTAD/MoO_3/Au were assembled. The resulting Sn–Ge PNC-based devices show a champion PCE of 4.9% with negligible hysteresis. Moreover, the introduction of Ge can help the improvement of long-term stability because of the inhibition of Sn^{2+} oxidation.

Conclusion and outlook

In summary, all-inorganic mixed group IVA cation perovskites have attracted growing attention due to their potentially high stability and environmental friendliness, leading to promising device performance parameters as presented in Table 1. Nevertheless, there is still a significant gap between their actual device performance and that of state-of-the-art perovskites. We envision that future research efforts in the following directions will contribute to filling the gap.

From the perspective of materials science, understanding and tailoring morphological defects such as grain boundaries, intragrain defects, and surfaces/heterointerfaces in these perovskites are critical to optimizing the properties and device performance. The inclusion of Sn and Ge cations has been found to significantly influence crystallization kinetics, while the mechanisms have not been elucidated. Multimodal characterization techniques with high spatiotemporal resolutions concerning the particular material characteristics of these perovskites needs to be developed and employed.

From the perspective of device sciences, the relatively high V_{OC} deficit needs to be addressed *via* novel interface designs. Particularly, perovskites containing Sn or Ge cations generally produce narrower bandgaps and thus wider light absorption than pure Pb perovskites, making the J_{SC} of the resulting devices advantageous. However, these perovskites tend to exhibit higher trap densities and less ideal band alignments in devices, leading to more severe non-radiative recombination. In this context, creating benign device interfaces with a range of organic, inorganic, and hybrid materials is necessary to overcome the V_{OC} bottleneck. In addition to generic interface design rules, we should take the unique oxidation issues for Sn or Ge into consideration.

Conflicts of interest

There are no conflicts to declare.

Acknowledgements

Z. Z., Y. L. and W. J. thank the Taishan Scholars Project of Shandong Province (Grant No. 201909121) and the Introduction and Cultivation Plan of Young Innovative Talents in Colleges and Universities of Shandong Province

(2019). Y. Z., T. D. and C. Y. acknowledge the Early Career Scheme (No. 22300221), the General Research Fund (No. 12302822) from the Hong Kong Research Grant Council (RGC), and the Excellent Young Scientists Funds (No. 52222318) from the National Natural Science Foundation of China. Y. Z., T. D. and C. Y. also acknowledge the start-up grants, Initiation Grant – Faculty Niche Research Areas (RC-FNRA-IG/20-21/SCI/06), Interdisciplinary Research Matching Scheme (IRMS/20-21/02) and Matching Proof-of-Concept Fund (MPCF-001-2022-23) of HKBU. T. D. acknowledges the support from the Hong Kong RGC Postdoctoral Fellowship.

References

1 K. Galkowski, A. Mitioglu, A. Miyata, P. Plochocka, O. Portugall, G. E. Eperon, J. T. W. Wang, T. Stergiopoulos, S. D. Stranks, H. J. Snaith and R. J. Nicholas, *Energy Environ. Sci.*, 2016, **9**, 962–970.
2 T. Baikie, Y. Fang, J. M. Kadro, M. Schreyer, F. Wei, S. G. Mhaisalkar, M. Grätzel and T. J. White, *J. Mater. Chem. A*, 2013, **1**, 5628–5641.
3 Q. Dong, Y. Fang, Y. Shao, P. Mulligan, J. Qiu, L. Cao and J. Huang, *Science*, 2015, **347**, 967–970.
4 J. Tong, Z. Song, D. H. Kim, X. Chen, C. Chen, A. F. Palmstrom, P. F. Ndione, M. O. Reese, S. P. Dunfield, O. G. Reid, J. Liu, F. Zhang, S. P. Harvey, Z. Li, S. T. Christensen, G. Teeter, D. Zhao, M. M. Al-Jassim, M. F. A. M. V. Hest, M. C. Beard, S. E. Shaheen, J. J. Berry, Y. Yan and K. Zhu, *Science*, 2019, **364**, 475–479.
5 D. Ma, K. Lin, Y. Dong, H. Choubisa, A. H. Proppe, D. Wu, Y. Wang, B. Chen, P. Li, J. Z. Fan, F. Yuan, A. Johnston, Y. Liu, Y. Kang, Z. H. Lu, Z. Wei and E. H. Sargent, *Nature*, 2021, **599**, 594–598.
6 R. Lin, J. Xu, M. Wei, Y. Wang, Z. Qin, Z. Liu, J. Wu, K. Xiao, B. Chen, S. M. Park, G. Chen, H. R. Atapattu, K. R. Graham, J. Xu, J. Zhu, L. Li, C. Zhang, E. H. Sargent and H. Tan, *Nature*, 2022, **603**, 73–78.
7 X. Lin, H. Su, S. He, Y. Song, Y. Wang, Z. Qin, Y. Wu, X. Yang, Q. Han, J. Fang, Y. Zhang, H. Segawa, M. Grätzel and L. Han, *Nat. Energy*, 2022, **7**, 520–527.
8 X. Zhao, T. Liu, Q. C. Burlingame, T. Liu, R. Holleylll, G. Cheng, N. Yao, F. Gao and Y.-L. Loo, *Science*, 2022, **377**, 307–310.
9 K. Xiao, Y.-H. Lin, M. Zhang, R. D. J. Oliver, X. Wang, Z. Liu, X. Luo, J. Li, D. Lai, H. Luo, R. Lin, J. Xu, Y. Hou, H. J. Snaith and H. Tan, *Science*, 2022, **376**, 762–767.
10 Z. Li, B. Li, X. Wu, S. A. Sheppard, S. Zhang, D. Gao, N. J. Long and Z. Zhu, *Science*, 2022, **376**, 416–420.
11 X. Li, W. Zhang, X. Guo, C. Lu, J. Wei and J. Fang, *Science*, 2022, **375**, 434–437.
12 N. Li, X. Niu, L. Li, H. Wang, Z. Huang, Y. Zhang, Y. Chen, X. Zhang, C. Zhu, H. Zai, Y. Bai, S. Ma, H. Liu, X. Liu, Z. Guo, G. Liu, R. Fan, H. Chen, J. Wang, Y. Lun, X. Wang, J. Hong, H. Xie, D. S. Jakob, X. G. Xu, Q. Chen and H. Zhou, *Science*, 2021, **373**, 561–567.
13 Y. Zou, P. Teng, W. Xu, G. Zheng, W. Lin, J. Yin, L. Kobera, S. Abbrent, X. Li, J. A. Steele, E. Solano, M. B. J. Roeffaers, J. Li, L. Cai, C. Kuang, I. G. Scheblykin, J. Brus, K. Zheng, Y. Yang, O. F. Mohammed, O. M. Bakr, T. Pullerits, S. Bai, B. Sun and F. Gao, *Nat. Commun.*, 2021, **12**, 4831.
14 W. Kim, H. Kim, T. J. Yoo, J. Y. Lee, J. Y. Jo, B. H. Lee, A. A. Sasikala, G. Y. Jung and Y. Pak, *Nat. Commun.*, 2022, **13**, 720.
15 Y. J. Li, Y. Lv, C.-L. Zou, W. Zhang, J. Yao and Y. S. Zhao, *J. Am. Chem. Soc.*, 2016, **138**(7), 2122–2125.
16 A. Kojima, K. Teshima, Y. Shirai and T. Miyasaka, *J. Am. Chem. Soc.*, 2009, **131**(17), 6050–6051.
17 **https://www.nrel.gov/pv/cell-efficiency.html**.
18 J. Huang, S. Tan, P. D. Lund and H. Zhou, *Energy Environ. Sci.*, 2017, **10**, 2284–2311.
19 T. Leijtens, K. Bush, R. Cheacharoen, R. Beal, A. Bowring and M. D. McGehee, *J. Mater. Chem. A*, 2017, **5**, 11483–11500.
20 E. T. Hoke, D. J. Slotcavage, E. R. Dohner, A. R. Bowring, H. I. Karunadasa and M. D. McGehee, *Chem. Sci.*, 2015, **6**, 613–617.
21 J. A. Christians, P. Schulz, J. S. Tinkham, T. H. Schloemer, S. P. Harvey, B. J. T. de Villers, A. Sellinger, J. J. Berry and J. M. Luther, *Nat. Energy*, 2018, **3**, 68–74.
22 Y. Wang, M. I. Dar, L. K. Ono, T. Zhang, M. Kan, Y. Li, L. Zhang, X. Wang, Y. Yang, X. Gao, Y. Qi, M. Grätzel and Y. Zhao, *Science*, 2019, **365**, 591–595.
23 P. Wang, X. Zhang, Y. Zhou, Q. Jiang, Q. Ye, Z. Chu, X. Li, X. Yang, Z. Yin and J. You, *Nat. Commun.*, 2018, **9**, 2225.
24 X. Sun, Z. Shao, Z. Li, D. Liu, C. Gao, C. Chen, B. Zhang, L. Hao, Q. Zhao, Y. Li, X. Wang, Y. Lu, X. Wang, G. Cui and S. Pang, *Joule*, 2022, **6**, 850–860.
25 M. Kulbak, D. Cahen and G. Hodes, *J. Phys. Chem. Lett.*, 2015, **6**, 2452–2456.
26 Y. Cui, J. Shi, F. Meng, B. Yu, S. Tan, S. He, C. Tan, Y. Li, H. Wu, Y. Luo, D. Li and Q. Meng, *Adv. Mater.*, 2022, **34**, 2205028.
27 J. Rödel, W. Jo, K. T. P. Seifert, E.-M. Anton, T. Granzow and D. Damjanovic, *J. Am. Chem. Soc.*, 2009, **92**, 1153–1177.
28 J. Tian, Q. Xue, Q. Yao, N. Li, C. J. Brabec and H.-L. Yip, *Adv. Energy Mater.*, 2020, **10**, 2000183.
29 Q. Tai, K.-C. Tang and F. Yan, *Energy Environ. Sci.*, 2019, **12**, 2375–2405.
30 M. B. Faheem, B. Khan, C. Feng, M. U. Farooq, F. Raziq, Y. Xiao and Y. Li, *ACS Energy Lett.*, 2020, **5**(1), 290–320.
31 J. Chen and W. C. H. Choy, *Sol. RRL*, 2020, **4**, 2000408.
32 Y. Yuan, G. Yan, R. Hong, Z. Liang and T. Kirchartz, *Adv. Mater.*, 2022, **34**, 2108132.
33 J. Liang and Y. B. Qi, *Mater. Today Nano*, 2021, **16**, 100143.
34 O. O. Bello and M. E. Emetere, *Sol. Energy*, 2022, **243**, 370–380.
35 M. Ikram, R. Malik, R. Raees, M. Imran, F. Wang, S. Ali, M. Khan, Q. Khan and M. Maqbool, *Sustain. Energy Technol. Assess.*, 2022, **53**, 102433.
36 A. Wang, C. Zuo, X. Niu, L. Ding, J. Ding and F. Hao, *Chem. Eng. J.*, 2023, **451**, 138926.
37 H. Wei, P. Qiu, Y. Li, Y. Li, M. Peng, X. Zheng and X. Liu, *Ceram. Int.*, 2022, **48**, 5876–5891.

38 M. Zhu, C. Li, B. Li, J. Zhang, Y. Sun, W. Guo, Z. Zhou, S. Pang and Y. Yan, *Mater. Horiz.*, 2020, **7**, 2208–2236.
39 J. Y. Kim, J.-W. Lee, H. S. Jung, H. Shin and N.-G. Park, *Chem. Rev.*, 2020, **120**(15), 7867–7918.
40 A. Marronnier, G. Roma, S. Boyer-Richard, L. Pedesseau, J.-M. Jancu, Y. Bonnassieux, C. Katan, C. C. Stoumpos, M. G. Kanatzidis and J. Even, *ACS Nano*, 2018, **12**(4), 3477–3486.
41 R. J. Sutton, M. R. Filip, A. A. Haghighirad, N. Sakai, B. Wenger, F. Giustino and H. J. Snaith, *ACS Energy Lett.*, 2018, **3**(8), 1787–1794.
42 Z. Xiao, Y. Zhou, H. Hosono, T. Kamiya and N. P. Padture, *Chem. – Eur. J.*, 2018, **24**, 2305–2316.
43 M. H. Kumar, S. Dharani, W. L. Leong, P. P. Boix, R. R. Prabhakar, T. Baikie, C. Shi, H. Ding, R. Ramesh, M. Asta, M. Grätzel, S. G. Mhaisalkar and N. Mathews, *Adv. Mater.*, 2014, **26**, 7122–7127.
44 T. C. Jellicoe, J. M. Richter, H. F. J. Glass, M. Tabachnyk, R. Brady, S. E. Dutton, A. Rao, R. H. Friend, D. Credgington, N. C. Greenham and M. L. Böhm, *J. Am. Chem. Soc.*, 2016, **138**, 2941–2944.
45 X. Wu, W. Song, Q. Li, X. Zhao, D. He and Z. Quan, *Chem. – Asian J.*, 2018, **13**, 1654–1659.
46 M. N. Islam, J. Podder and M. L. Ali, *RSC Adv.*, 2021, **11**, 39553–39563.
47 F. Hao, C. C. Stoumpos, R. P. H. Chang and M. G. Kanatzidis, *J. Am. Chem. Soc.*, 2014, **136**(22), 8094–8099.
48 A. Rajagopal, R. J. Stoddard, H. W. Hillhouse and A. K.-Y. Jen, *J. Mater. Chem. A*, 2019, **7**, 16285–16293.
49 H. A. Schwartz, H. Laurenzen, A. Marzouk, M. Runkel, K. O. Brinkmann, D. Rogalla, T. Riedl, S. Ashhab and S. Olthof, *ACS Appl. Mater. Interfaces*, 2021, **13**, 4203–4210.
50 S. Tao, I. Schmidt, G. Brocks, J. Jiang, I. Tranca, K. Meerholz and S. Olyhof, *Nat. Commun.*, 2019, **10**, 2560.
51 R. M. I. Bandara, S. M. Silva, C. C. L. Underwood, K. D. G. I. Jayawardena, R. A. Sporea and S. R. P. Silva, *Energy Environ. Mater.*, 2022, **5**, 370–400.
52 D. J. Slotcavage, H. I. Karunadasa and M. D. McGehee, *ACS Energy Lett.*, 2016, **1**, 1199–1205.
53 L. A. Muscarella, E. M. Hutter, F. Wittmann, Y. W. Woo, Y.-K. Jung, L. McGovern, J. Versluis, A. Walsh, H. J. Bakker and B. Ehrler, *ACS Energy Lett.*, 2020, **5**, 3152–3158.
54 M. Hu, G. Wang, Q. Zhang, J. Gong, Z. Xing, J. Gao, J. Wang, P. Zeng, S. Zheng, M. Liu, Y. Zhou and S. Yang, *J. Energy Chem.*, 2022, **72**, 487–494.
55 H. Yan, J. Huang, X. Zhang, M. Wang, J. Liu, C. Meng, S. Deng, L. Lu, P. Xu, H.-S. Kwok and G. Li, *Sol. RRL*, 2022, **6**, 2100899.
56 C.-H. Kuan, H.-H. Shen and C.-F. Lin, *RSC Adv.*, 2021, **11**, 3264–3271.
57 A. Swarnkar, W. J. Mir and A. Nag, *ACS Energy Lett.*, 2018, **3**, 286–289.
58 S. Lee, J. Moon, J. Ryu, B. Parida, S. Yoon, D.-G. Lee, J. S. Cho, S. Hayase and D.-W. Kang, *Nano Energy*, 2020, **77**, 105309.
59 J. Liang, P. Zhao, C. Wang, Y. Wang, Y. Hu, G. Zhu, L. Ma, J. Liu and Z. Jin, *J. Am. Chem. Soc.*, 2017, **139**(40), 14009–14012.
60 N. Y. Nia, F. Giordano, M. Zendehdel, L. Cinà, A. L. Palma, P. G. Medaglia, S. M. Zakeeruddin, M. Grätzel and A. D. Carlo, *Nano Energy*, 2020, **69**, 104441.
61 T. Salim, S. Sun, Y. Abe, A. Krishna, A. C. Grimsdale and Y. M. Lam, *J. Mater. Chem. A*, 2015, **3**, 8943–8969.
62 N. Li, Z. Zhu, J. Li, A. K.-Y. Jen and L. Wang, *Adv. Energy Mater.*, 2018, **8**, 1800525.
63 Z. Yang, X. Zhang, W. Yang, G. E. Eperon and D. S. Ginger, *Chem. Mater.*, 2020, **32**(7), 2782–2794.
64 M. Hu, M. Chen, P. Guo, H. Zhou, J. Deng, Y. Yao, Y. Jiang, J. Gong, Z. Dai, Y. Zhou, F. Qian, X. Chong, J. Feng, R. D. Schaller, K. Zhu, N. P. Padture and Y. Zhou, *Nat. Commun.*, 2020, **11**, 151.
65 Z. Zhou, Z. Qiang, T. Sakamaki, I. Takei, R. Shang and E. Nakamura, *ACS Appl. Mater. Interfaces*, 2019, **11**(25), 22603–22611.
66 J. Zhan, M. Li and Z. Zhou, *Sol. RRL*, 2022, 2200082.
67 Y. Ahmed, B. Khan, M. B. Faheem, K. Huang, Y. Gao and J. Yang, *J. Energy Chem.*, 2022, **67**, 361–390.
68 G. Chen, P. Li, T. Xue, M. Su, J. Ma, Y. Zhang, T. Wu, L. Han, M. Aldamasy, M. Li, Z. Li, J. Ma, S. Chen, Y. Zhao, F. Wang and Y. Song, *Small*, 2021, **17**, 2101380.
69 W. Zhang, H. Liu, X. Qi, Y. Yu, Y. Zhou, Y. Xia, J. Cui, Y. Shi, R. Chen and H.-L. Wang, *Adv. Sci.*, 2022, **9**, 2106054.
70 E. W.-G. Diau, E. Jokar and M. Rameez, *ACS Energy Lett.*, 2019, **4**(8), 1930–1937.
71 J. Pascual, M. Flatken, R. Félix, G. Li, S.-H. Turren-Cruz, M. H. Aldamasy, C. Hartmann, M. Li, D. D. Girolamo, G. Nasti, E. Hüsam, R. G. Wilks, A. Dallmann, M. Bär, A. Hoell and A. Abate, *Angew. Chem., Int. Ed.*, 2021, **60**, 21583–21591.
72 T. M. Koh, T. Krishnamoorthy, N. Yantara, C. Shi, W. L. Leong, P. P. Boix, A. C. Grimsdale, S. G. Mhaisalkar and N. Mathews, *J. Mater. Chem. A*, 2015, **3**, 14996–15000.
73 S. J. Lee, S. S. Shin, Y. C. Kim, D. Kim, T. K. Ahn, J. H. Noh, J. Seo and S. I. Seok, *J. Am. Chem. Soc.*, 2016, **138**(12), 3974–3977.
74 H. Ban, Q. Sun, T. Zhang, H. Li, Y. Shen and M. Wang, *Sol. RRL*, 2020, **4**, 1900457.
75 A. Swarnk, A. R. Marshall, E. M. Sanehira, B. D. Chernomordik, D. T. Moore, J. A. Christians, T. Chakrabarti and J. M. Luther, *Science*, 2016, **354**, 92–95.
76 J. Yuan, C. Bi, J. Xi, R. Guo and J. Tian, *J. Phys. Chem. Lett.*, 2021, **12**(3), 1018–1024.
77 F. Liu, C. Ding, Y. Zhang, T. S. Ripolles, T. Kamisaka, T. Toyoda, S. Hayase, T. Minemoto, K. Yoshino, S. Dai, M. Yanagida, H. Noguchi and Q. Shen, *J. Am. Chem. Soc.*, 2017, **139**(46), 16708–16719.
78 T. Lei, M. Lai, Q. Kong, D. Lu, W. Lee, L. Dou, V. Wu, Y. Yu and P. Yang, *Nano Lett.*, 2018, **18**(6), 3538–3542.
79 I. Chung, J.-H. Song, J. Im, J. Androulakis, C. D. Malliakas, H. Li, A. J. Freeman, J. T. Kenney and M. G. Kanatzidis, *J. Am. Chem. Soc.*, 2012, **134**(20), 8579–8587.

80 F. Yang, D. Hirotani, G. Kapil, M. A. Kamarudin, C. H. Ng, Y. Zhang, Q. Shen and S. Hayase, *Angew. Chem., Int. Ed.*, 2018, **57**, 12745–12749.
81 L. Wang, J. Su, Y. Guo, Z. Lin, Y. Hao and J. Chang, *J. Phys. Chem. Lett.*, 2021, **12**(3), 1098–1103.
82 M. Chen, M.-G. Ju, H. F. Garces, A. D. Carl, L. K. Ono, Z. Hawash, Y. Zhang, T. Shen, Y. Qi, R. L. Grimm, D. Pacifici, X. C. Zeng, Y. Zhou and N. P. Padture, *Nat. Commun.*, 2019, **10**, 16.
83 F. Valadares, I. Guilhon, L. K. Teles and M. Marques, *J. Phys. Chem. C*, 2021, **125**(39), 21740–21747.
84 J. Chang, L. Jiang, G. Wang, W. Zhao, Y. Huang and H. Chen, *Phys. Chem. Chem. Phys.*, 2021, **23**, 14449–14456.
85 Y. Raoui, S. Kazim, Y. Galagan, H. Ez-Zahraouyc and S. Ahmad, *Sustainable Energy Fuels*, 2021, **5**, 4661–4667.
86 M. Liu, H. Pasanen, H. Ali-Löytty, A. Hiltunen, K. Lahtonen, S. Qudsia, J.-H. Smått, M. Valden, N. V. Tkachenko and P. Vivo, *Angew. Chem., Int. Ed.*, 2020, **59**, 22117–22125.